Bioactive Materials 6 (2021) 2158–2172

Contents lists available at ScienceDirect

Bioactive Materials

journal homepage: www.sciencedirect.com/journal/bioactive-materials

Antibody-activated trans-endothelial delivery of mesoporous organosilica nanomedicine augments tumor extravasation and anti-cancer immunotherapy

Tinglei Huang [a,1], Shuang Li [b,1], Jianchen Fang [c], Fuli Li [a], Shuiping Tu [a,*]

[a] Department of Oncology, State Key Laboratory of Oncogenes and Related Genes, Renji Hospital, School of Medicine, Shanghai Jiao Tong University, Shanghai, 200127, China
[b] Department of Stomatology, Renji Hospital, School of Medicine, Shanghai Jiao Tong University, Shanghai, 200127, China
[c] Department of Pathology, Renji Hospital, School of Medicine, Shanghai Jiao Tong University, Shanghai, 200127, China

ARTICLE INFO

Keywords:
Active transcytosis
Extravasation
Drug delivery
Cancer immunotherapy
Stimulus-responsive nanomedicine

ABSTRACT

Tumor vasculature constitutes a formidable hurdle for the efficient delivery of cancer nanomedicine into tumors. The leverage of passive pathway through inter-endothelial gaps in tumor blood vessels might account for limited extravasation of nanomedicine into tumor microenvironment (TME). Herein, Annexin A1 antibody-installed mesoporous organosilica nanoplatforms carrying immunotherapeutics of anti-PD-L1 antibody (aPD-L1) and Indoximod are developed to target at caveolar Annexin-A1 protein of luminal endothelial cells and to trigger the active *trans*-endothelial transcytosis of nanomedicine mediated by caveolae. Such strategy enables rapid nanomedicine extravasation across tumor endothelium and relatively extensive accumulation in tumor interstitium. aPD-L1 and Indoximod release from aPD/IND@MON-aANN in a reduction-responsive manner and synergistically facilitate the intratumoral infiltration of cytotoxic T lymphocytes and reverse the immunosuppressive TME, thus demonstrating substantial anti-tumor efficacy in subcutaneous 4T1 breast tumors and remarkable anti-metastatic capacity to extend the survival of 4T1 tumor metastasis model. Moreover, aPD/IND@MON-aANN nanomedicine also exhibits distinct superiority over the combination therapy of free drugs to potently attenuate the progression of urethane-induced orthotopic lung cancers. Collectively, aPD/IND@MON-aANN nanoplatforms with boosted delivery efficiency via antibody-activated *trans*-endothelial pathway and enhanced immunotherapeutic efficacy provides perspectives for the development of cancer nanomedicines.

1. Introduction

Cancer nanomedicines have been enormously developed over the past three decades, yet scarce nanotherapeutics have been approved for clinical trials and most of them have demonstrated poor therapeutic efficacy [1–3]. The compromised potency of nanomedicines has been attributed to the limited delivery efficiency into tumors, with less than ~1% of the nanoparticle dose reaching solid tumors after systemic administration in animal models [4]. Tumor vasculature constitutes a formidable biological barrier for the entry of nanomedicines into tumor tissue and insufficient extravasation across the vascular barrier greatly hampers the delivery efficiency and efficacy of nanotherapeutics [5]. The conventionally accepted rationale for nanoparticle extravasation is the passive diffusion route through the inter-endothelial gaps in tumor endothelium, namely, the enhanced retention and permeability (EPR) effect [6,7]. However, it has been recently unveiled that the active delivery of nanoparticles mediated by cellular transcytosis accounts for the dominant mechanism for the nanoparticle entry into solid tumors instead of the passive mechanism [8]. Therefore, the harness of active transcytosis in tumor endothelium for nanomedicine development could be a promising strategy to enhance extravasation and accumulation of nanomedicines in TME.

To date, the exact mechanism and triggering factors of active transcytosis still remain largely unknown. Polymer–drug conjugates were reported to exploit the cationization process to induce adsorption-mediated active transcytosis, thus enabling *trans*-endothelial and

Peer review under responsibility of KeAi Communications Co., Ltd.
* Corresponding author.
E-mail address: tushuiping@yahoo.com (S. Tu).
[1] Tinglei Huang and Shuang Li contributed equally to this work.

https://doi.org/10.1016/j.bioactmat.2020.12.023
Received 18 August 2020; Received in revised form 23 December 2020; Accepted 28 December 2020

transcellular transport and uniform distribution throughout the tumors [9]. Earlier fundamental work suggested that the caveolae-mediated endocytosis and the active translocation across endothelium could occur when certain glycoproteins enriched in caveolae were activated by corresponding ligands [10–12]. Among them, Annexin A1 (ANXA1) was proven to be specifically upregulated in the endothelium of multiple tumors rather than that of normal tissues [12]. For development of nanomedicines with targeting property, a major strategy is to functionalize the nanocarrier surface with certain ligands, such as antibodies and peptides, to steer their delivery to particular tissues [13]. Nevertheless, the targeting of tumor vasculature and activation of transcytosis of nanomedicine across tumor endothelium via ligand approaches for active *trans*-vascular delivery of nanocarriers still remain largely unexplored.

Anti-PD-1/PD-L1 immune checkpoint blockade (ICB) immunotherapy has exhibited huge potential for the treatment of cancers such as melanoma and microsatellite instable cancers, yet the response rates for the bulk of indications still stay rather low, especially for solid tumors [14,15]. For one thing, the systemic administration dosing of ICB antibodies is limited due to the autoimmune-type safety concerns meanwhile only a small fraction of the administered dose reaches specific tumor sites. Hence, nanocarriers devised to improve tumor extravasation and accumulation could offer a solution to ensure the relatively potent payloads of ICB antibodies concentrated on tumor tissues to maximize the therapeutic outcome. For another, myriad immunosuppressive factors in TME tend to induce T cell dysfunction upon the infiltration of T cells, thus greatly limiting the potential of tumor immunotherapy [16,17]. Among them, the catabolism of tryptophan mediated by indole 2,3-dioxygenase(IDO) in TME has increasingly been shown to fundamentally interfere with T cell functions [18]. Hence, the combination of the IDO inhibitor — Indoximod and aPD-L1 equipped in the nanoplatforms could serve to overcome hurdles posed by TME and boost immunotherapy efficacy.

2. Material and methods

2.1. Materials

Purpald, Urethane, DNase I and collagenase IV were purchased from Sigma–Aldrich. anti-CD3-BV650, anti-CD8a-FITC, anti–IFN–γ-APC, anti-CD45-PE-Cy7, anti-CD3-FITC, anti-CD4-PerCP-Cy5.5, anti-CD25-PE, anti-FOXP3-APC, anti-aPD-L1-PE antibodies and Fixable Viability Stain 510, fixable viability stain780, FcγR blocking were brought from BD Biosciences. FOXP3-APC antibody was purchased from eBioscience. Cetyltrimethylammonium chloride (CTAC), triethanolamine (TEA), Tetraethyl orthosilicate (TEOS), succinic anhydride, 2-(*N*-morpholino) ethanesulfonic acid (MES), (3-Aminopropyl) triethoxysilane (APTES) were purchased from Aladdin Chemistry. Bis (triethoxysilylpropyl) disulfide (BTES), 1-ethyl-3-(3-dimethly-aminopropyl) carbodiimide (EDC), *N*-hydroxysuccinimide (NHS), Fluorescein 5(6)-isothiocyanate (FITC), Sodium phosphate monobasic (Na_2HPO_4), Sodium periodate ($NaIO_4$), sodium triacetoxyborohydride, Cy5-amine, glutathione (GSH) and HEPES were obtained from Macklin Chemistry. 10 k MWCO centrifuge filter was purchased from Millipore. Simulated body fluid (SBF) was bought from Leagene Biotechnology Co., Ltd. Amino PEG Acid was bought from Ponsure Biological. InVivoMab anti-mouse PD-L1 (B7–H1) was brought from Bio X Cell. Indoximod were purchased from MCE. IgG Isotype Control, anti-rat IgG total ELISA kit was obtained from R&D Systems. IRDye 680RD secondary antibody was bought from LI-COR Biosciences. Trypsin-EDTA, RPMI-1640, Dulbecco's Modified Eagle Medium (DMEM), fetal bovine serum (FBS) and penicillin/streptomycin were bought from Gibco-BRL. 6 nm colloidal gold secondary antibody was purchased from Jackson ImmunoResearch. Cell Counting Kit-8 (CCK-8) was bought from Dojindo Laboratories. Mounting Medium with DAPI, anti-CD31 antibody were purchased from abcam. anti-ANXA1 was purchased from GeneTex. Endothelial Cell Medium (ECM) was purchased from ScienceCell. genistein and EXO1 were bought from MCE.

2.2. The synthesis and characterization of MONs

MONs inserted with disulfide were synthesized according to previously reported protocol [19]. Briefly, 2 g cetyltrimethylammonium chloride (CTAC) and 0.06 g triethanolamine (TEA) were added into 20 ml dH_2O under magnetic stirring at RT for 15 min and transferred to thermostatic oil bath at 80 °C for use. Meanwhile 1 ml tetraethyl orthosilicate (TEOS) and 0.2 ml bis (triethoxysilylpropyl) disulfide (BTES) were mixed well by sonication prior to addition to the above solution by dropwise. The mixture was stirred in thermostatic oil bath at 80 °C for 4 h. The MONs were collected after centrifugation at 21 000 g for 15 min and washed with ethyl alcohol and dH_2O twice. Afterwards, the surfactants (CTAC) in the obtained MONs were removed by stirring in solution of sodium chloride in methanol (8 mg/ml). For the characterization of the as-synthesized MONs, the morphology was observed via TEM (Talos L120C, Thermo Fisher Scientific), the hydrodynamic size distribution was measured by dynamic light scattering (DLS, zetasizer, Malvern). The pore size distribution and surface area of MONs were calculated from Nitrogen adsorption-desorption isotherm results (NOVA 4200e, Quantachrome).

For the preparation of MONs functionalized with amine groups and carboxy groups, firstly, APTES were added to dispersed MONs in ethyl alcohol to reflux for 24 h to obtain MONs with amino terminals (denoted MON-NH_2). Then MON-NH_2 nanoparticles were reacted with succinic anhydride dissolved in DMF for 24 h at RT to get carboxy-modified MONs (MON-COOH). To confirm the successive grafting of the amine groups and carboxy groups, MON, MON-NH_2 and MON-COOH samples were taken for zeta potential measurement via DLS. For fluorescent assays, MON-COOH nanoparticles were further labelled with FITC [20]. Briefly, FITC-APTES was initially prepared by the addition of excessive FITC to APTES in ethyl alcohol to react for 24 h in dark. The FITC-APTES was then mixed with dispersed MON-COOH nanoparticles to reflux for 24 and washed for further steps. For biodistribution study, MON-COOH nanoparticles were linked with Cy5-amine via EDC-NHS reaction. Briefly, 10 mg nanoparticles were dispersed and sonicated in MES buffer (50 mM, pH 5.6), then 4.8 mg EDC and 7.19 mg NHS pre-dissolved in MES buffer were added to the nanoparticle solution to stir for 20 min in dark at RT to activate the carboxy groups on MON-COOH nanoparticles. Afterwards, 2 mg Cy5-amine were added into the mixture for overnight crosslinking. The obtained nanoparticles were then washed for further use.

2.3. The synthesis and characterization of aPD/IND@MON-aANN

The Amino PEG Acid (NH_2-PEG-COOH, MV2000) was used as a heterobifunctional linker for the immobilization of Annexin A1 antibodies (aANXA1) to MON-COOH. The antibody–linker complex was prepared according to previous protocol [21]. The solution of aANXA1 or IgG antibody (1 mg/ml) was resuspended in 100 μl 100 mM Na_2HPO_4 buffer (pH 7.5) and 10 μl of 100 mM $NaIO_4$ were added to oxidize the carbohydrate in antibodies in dark for 30 min at RT, followed by the reaction quenching by PBS. The presence of reactive aldehydes from the oxidation process was indicated by the Purpald solution. Then the antibody solution was reacted to the linker solution (2 μl, 50 mM) containing primary amine ends under stirring at 4 °C for 20 h followed by the addition of sodium triacetoxyborohydride solution into the mixture at RT for another 4 h. The obtained antibody – linker solution was washed and filtered with 40 mM HEPES buffer via 10 k MWCO centrifuge filter and resuspend in 1 ml buffer for further nanoparticle linking. The antibody – linker complex or pure PEG linker solution were immobilized to the functionalized MONs by the reaction between the carboxy terminals on the linker of the complex and the amines on the MONs through EDC and NHS. Briefly, 100 μl of the above antibody –

linker sample or pure PEG linker solution was resuspended in MES buffer (50 mM, pH 5.6) followed by the addition of 0.1 mg EDC and 0.15 mg NHS pre-dissolved in MES buffer. The reaction was stirred for 20 min in dark at RT prior to the addition of 5 mg the functionalized MONs dispersed in PBS and overnight crosslinking. The obtained nanoparticles, including those without further decoration (denoted MON-COOH), with PEG conjugation (denoted MON-PEG), with conjugation of PEG-IgG complexes (denoted MON-PEG-IgG) and with conjugation of PEG-aANN complexes (denoted MON-PEG-aANN), were then washed with PBS for three times for further experiments.

Subsequently, 200 μg murine PD-L1 antibody was directly immobilized to the surface of 5 mg above nanoparticles via the above-mentioned EDC reaction between the free carboxy groups on nanoparticles and the amino groups on aPD-L1. The obtained nanoparticles conjugated with aPD-L1 were denoted aPD@MON-COOH, aPD@MON-PEG, aPD@MON-IgG and aPD@MON-aANN, respectively. Moreover, the grafting efficiency of aPD-L1 for aANXA1-installed nanocarrier group was determined by measuring the non-conjugated aPD-L1 content in the supernatant collected at the end of the conjugation assay by an anti-rat IgG total ELISA kit. For the loading of Indoximod into the above nanocarriers, 5 mg of the above nanocarriers was added to the Indoximod solution in PBS (10 ml, 1 mg/ml) and sonicated intermittently on ice for 15 min. The mixture was then subjected to magnetic stirring for 24 h in dark. The nanoparticles were obtained by centrifugation at 21 000 g for 15 min. The nanoparticles simultaneously involved with aPD-L1 and Indoximod were denoted aPD/IND@MON-COOH, aPD/IND@MON-PEG, aPD/IND@MON-IgG and aPD/IND@MON-aANN, respectively. To evaluate the encapsulation efficiency of Indoximod of aPD/IND@MON-aANN, the supernatant was collected to determine the residual Indoximod content according to the calibration curve of Indoximod standard solutions via HPLC analysis (Agilent Technologies, 1260 Infinity II).

To confirm the attachment of antibody–linker complex to MON-COOH, aANXA1 was directly immobilized to the MONs through EDC/NHS reaction as a control (denoted MON-aANN). Then samples from functionalized MON-COOH, MON-aANN, MON-PEG-aANN group were analyzed by DLS. To verify the conjugation of aANXA1 and aPD-L1 on aPD@MON-aANN, IRDye 680RD-labelled aANXA1 and PE-labelled aPD-L1 were similarly attached to FITC-labelled MON-COOH, followed by examination by fluorescence spectrometer (FluroMax-4, HORIBA). Moreover, the morphology of aPD/IND@MON-aANN was observed via TEM.

2.4. In vitro release of indoximod and aPD-L1 from aPD/IND@MON-aANN

To assess the in vitro drug release from aPD/IND@MON-aANN, 1 mg nanoparticles were added to 1 ml SBF solution with varying GSH concentration (GSH = 0 mM and 10 mM) in dialysis bags. The releasing equipment was shaken at 150 rpm at 37 °C and the release solution was collected at certain time points within 48 h and replenished with fresh medium. The content of the released Indoximod was determined based on the above calibration curve by HPLC. Released aPD-L1 was collected by ultracentrifugation and measured by ELISA (R&D systems). The release assays were conducted in triplicates. Moreover, the degradation products of aPD/IND@MON-aANN for release tests after 48 h were further collected for TEM observation and DLS measurement.

2.5. The immunofluorescence assay of ANXA1 and CD31 colocalization

To detect the expression of ANXA1 on tumor endothelium, mouse normal lung tissue, tumor samples of mouse 4T1 breast cancers, human breast cancers and lung cancers were fixed with 4% formaldehyde, embedded and cut into tissue sections. Then, the sections were stained with antibodies for ANXA1 and CD31, a marker for endothelial cells, followed by staining with the corresponding fluorescent secondary antibodies and DAPI for cell nuclei. The immunofluorescent staining sections were then imaged by confocal microscopy (Zeiss LSM 880) to observe the colocalization of CD31 (green) and Annexin A1 (red). The experiments using human tumor tissue samples were conducted in compliance with ethical guidelines approved by Institutional Ethical Review Committee of Renji Hospital, School of Medicine of Shanghai Jiao Tong University. The participating patients consented to the use of biospecimens for research purpose. The fluorescence intensity of ANXA1 localized at the CD31 positive zone for various tissue samples as well as were analyzed via Image J. For the quantification of the co-localization between ANXA1 and CD31, Manders' co-localization coefficients denoting the fraction of CD31 overlapping with ANXA1 were analyzed via the co-localization plugin in Image J. The coefficient is close to 1 when they are highly co-localized.

2.6. Western blotting

The total protein of various HUVEC samples were extracted by protein lysis buffer. After being heat-denatured, the protein samples were subjected to SDS-PAGE running and subsequently electro-transferred to PVDF membrane. The PVDF membrane were blocked using 5% skim milk for 1 h at RT and then incubated with the specific primary antibodies against ANXA1 at 4 °C for 12 h. The membranes were washed three times and incubated with horseradish peroxidase labelled secondary antibodies at RT for 1 h. The membranes were washed three times and then the relative protein expression level was assessed by ECL chemical luminescence. β-actin was used as the loading control.

2.7. Nanoparticle transcytosis via a transwell cell-culture model

In vitro assays were conducted to detect the transcytosis of the aANXA1-decorated nanomedicine across tumor endothelial cells. Firstly, we generated a co-culture system by seeding 4T1 and HUVECs separately into the lower and upper transwells (diameter 0.4 μM; Corning, Shanghai, China), followed by western blotting analysis to determine the expression level of ANXA1 in the HUVECs cultured alone or co-cultured with 4T1. In this way, tumor endothlium would be simulated in vitro. After the confirmation of upregulated ANXA1 in co-cultured HUVECs, the obtained HUVECs were used to build an in vitro transcytosis model as previously described [22,23]. Briefly, 1×10^5 HUVECs were seeded onto gelatin-coated polyester membrane transwells with 0.4 μm pore size and cultured for 72 h to reach confluency, making sure that the transendothelial electrical resistance (TEER) was more than 30 Ohm × cm^2.

To investigate the capacity of aPD/IND@MON-aANN to traverse tumor endothelial cells, FITC-labelled aPD/IND@MON-aANN and aPD/IND@MON-IgG with equivalent fluorescence intensity were added to the upper chambers of the transcytosis models with HUVECs cultured alone or pretreated with 4T1 co-culture, respectively. After 60 min, the various culture medium in the lower chamber were collected and the fluorescence intensity was measured by a Fluorescence Spectrophotometer (Varioskan Flash, Thermo Scientific). To further determine the effects of transcellular inhibitors on the *trans*-endothelial transport of aPD/IND@MON-aANN, the co-cultured HUVECs were pretreated with or without 200 μM genistein (endocytic pathway inhibitor) or 20 μM EXO1 (exocytic pathway inhibitor) for 2 h. Afterwards, FITC-labelled aPD/IND@MON-aANN and aPD/IND@MON-IgG with equivalent fluorescence intensity were added to the upper chambers of the transcytosis models with HUVECs treated above. After 30 min and 60 min of incubation, the fluorescence intensity of liquid in the lower chambers was detected. Experiments were repeated in triplicates.

2.8. The biodistribution study

The biodistribution of nanoparticles was performed on BALB/c mice subcutaneously bearing 4T1 tumors. The mice were intravenously

injected with Cy5-labelled nanoparticles (200 μl) with equivalent fluorescence intensity, including aPD/IND@MON-COOH, aPD/IND@MON-PEG, aPD/IND@MON-IgG and aPD/IND@MON-aANN. After 8 h, the mice were sacrificed and the major organs including heart, liver, spleen, lung, kidney and tumor, were collected, washed with PBS and imaged by in vivo imaging system (IVIS) under the same settings. The fluorescence intensity was measured by Living Image software.

2.9. The extravasation of nanoparticles into 4T1 tumors in vivo

For real-time observation of in vivo tumor extravasation of various nanoparticles, nude mice bearing 4T1 tumors in the subcutaneous tissue of ears were adopted as the animal model [24]. After anesthesia, the tumor-bearing ears were put under the fluorescence microscopy (Olympus) and fixed by microscope slides to ensure the relatively flat and stable tumor surface, followed by tail vein injection with FITC-labelled nanoparticles (100 μl) with equivalent fluorescence intensity, including aPD/IND@MON-COOH, aPD/IND@MON-PEG, aPD/IND@MON-IgG and aPD/IND@MON-aANN. The real-time extravasation and accumulation of different formulations in tumor interstitium were monitored and imaged by fluorescence microscopy excited at 488 nm. The corresponding fluorescence intensity was analyzed via Image J.

2.10. TEM observation for the nanoparticle transport into tumor

aPD/IND@MON-aANN nanoparticles were firstly incubated with 6 nm colloidal gold secondary antibodies to aANXA1 at 4 °C for 24 h followed by PBS rinses. After TEM analysis to determine the successful conjugation of immunogold labels, the gold-conjugated aPD/IND@MON-aANN nanoparticles were then i.v. injected into tumor-bearing mice, 30 min later, tumor was separated and cut into small pieces which was subsequently fixed in 2.5% glutaraldehyde, 1% osmic acid for 2 h at 4 °C. After gradient dehydration, the samples were embedded with epoxy resin and cut into sections for TEM observation.

2.11. Cell culture

Murine 4T1, NIH-3T3, human 293T cells and Human Umbilical Vein Endothelial Cells (HUVECs) were purchased from the American Type Culture Collection. Cells were incubated in RPMI-1640 (4T1) or DMEM medium (NIH-3T3, 293T) or and ECM (HUVECs) with 10% fetal bovine serum (FBS) and 1% penicillin/streptomycin in a humidified atmosphere with 5% CO_2 at 37 °C.

2.12. Animals

6-8 weeks-old female BALB/c and C57BL/6 mice were obtained from and housed in specific pathogen-free (SPF) condition in the Animal Center at Renji Hospital. All animal procedures were carried out under the ethical guidelines approved by Institutional Animal Care and Use Committee of Renji Hospital, School of Medicine of Shanghai Jiao Tong University.

2.13. Anti-tumor activity in subcutaneous 4T1 tumors

5×10^5 4T1 cells were subcutaneously injected into the right flanks of 6–8 weeks-old female BALB/c mice. When the tumor volume reached approximately 50 mm^3, tumor-bearing mice were randomly grouped (n = 5) and administered with Isotype control antibody (10 mg kg^{-1}), free aPD-L1 (denoted "aPD", 10 mg kg^{-1}), aPD@MON-IgG nanoparticles (0.5 mg kg^{-1}), aPD@MON-aANN nanoparticles (0.5 mg kg^{-1}) and aPD/IND@MON-aANN nanoparticles (0.5 mg kg^{-1}) on day 7, 10, and 13 via tail vein injection. The tumor volume and mice body weight were measured every two days. The tumor bulk was calculated using the formula: $V = L \times W \times W/2$ (L, the longer dimension; W, the shorter dimension). At the end of the experiment, mice were sacrificed and peripheral blood serum was harvested to evaluate the serum levels hepatic, kidney, heart function parameters. Intratumoral infiltration of CTLs and Tregs was analyzed by flow cytometry meanwhile tumor tissue was imbedded and cut into sections for H&E staining and terminal deoxynucleotidyl transferase 2′-deoxyuridine 5′-triphosphate nick end labeling (TUNEL) staining. The major organs including heart, lung, liver, spleen and kidneys from various groups were also collected for H&E staining to evaluate the biocompatibility of nanoparticles.

2.14. Anti-metastasis efficacy

6-8 weeks-old female BALB/c mice were inoculated with 1×10^5 4T1 breast cancer cells stably transfected with luciferase via tail vein injection. 7 days after tumor inoculation, mice were grouped and intravenously administered with Isotype control antibody, free aPD-L1/IND(10 mg kg^{-1}), aPD/IND@MON-IgG (0.5 mg kg^{-1}) and aPD/IND@MON-ANN nanoparticles (0.5 mg kg^{-1}) on day 7, 10 and 13, respectively. The mice tumor metastasis was measured by in vivo imaging system (IVIS). Mice were sacrificed when the bioluminescence of any group exceeded 5×10^5 p s^{-1} cm^{-2} sr^{-1}. The main organs, including lung, liver, spleen, kidney, adrenal glands, mesentery, ovary and lymph node, of the sacrificed mice were then collected for H&E staining to confirm the cancer metastasis. The survival study was adopted to assess the comprehensive therapeutic effects of various formulations in an independent experiment.

2.15. Flow cytometric analysis of intratumoral infiltration of immune populations

4T1-tumors isolated from the sacrificed mice were cut into small fragments and immersed in the RPMI-1640 medium containing 0.2 mg/ml DNase I and 1 mg/ml collagenase IV and cultured at 37 °C for 45 min. Then the solution was filtered by the 70 μm filter to obtain single cell suspension. The single cell suspension was subjected to fixable viability staining and FcγR blocking, followed by incubation with various fluorescent-labelled antibodies according to manufacturer's protocol. Then, the samples were detected by flow cytometry (LSR Fortessa, BD Biosciences) and analyzed by FlowJo software. For the detection of CTLs, samples were stained with Fixable Viability Stain 510, anti-CD45-PE-Cy7, anti-CD3-BV650, anti-CD8-FITC, and anti–IFN–γ-APC antibodies. For the analysis of Tregs, samples were stained with fixable viability stain780, anti-CD45-PE-Cy7, anti-CD3-FITC, anti-CD4-PerCP-Cy5.5, anti-CD25-PE and anti-FOXP3-APC. The fraction of $CD3^+CD8^+$ population was calculated within the $CD45^+$ population, the fraction of $CD8^+IFN\text{-}\gamma^+$ population was calculated within the $CD3^+CD8^+$ population and the proportion of $CD25^+FOXP3^+$ population was calculated within the $CD4^+$ population. The total number of $CD3^+CD8^+$ population was analyzed by normalizing the percentage to tumor mass.

2.16. Anti-tumor efficacy in urethane-induced orthotopic lung cancers

6-8 week-old female C57BL/6 mice were administered intraperitoneally with urethane one dose per week (1 mg g^{-1} body weight) for 10 consecutive doses, as described previously [25]. 15 weeks after the first injection, tumor-bearing mice were randomly grouped (n = 8 per group) and treated with Isotype control antibody, free aPD-L1/IND(10 mg kg^{-1}), PD/IND@MON-IgG nanoparticles (0.5 mg kg^{-1}) and PD/IND@MON-ANN nanoparticles (0.5 mg kg^{-1}) every 3 days for 3 times via tail vein injection. Two weeks after the first dose, the tumor progression was examined by 18F-FDG microPET/CT (Siemens Inveon) and the lung tissue of the sacrificed mice were dissected for H&E staining for histological observation of tumor progression.

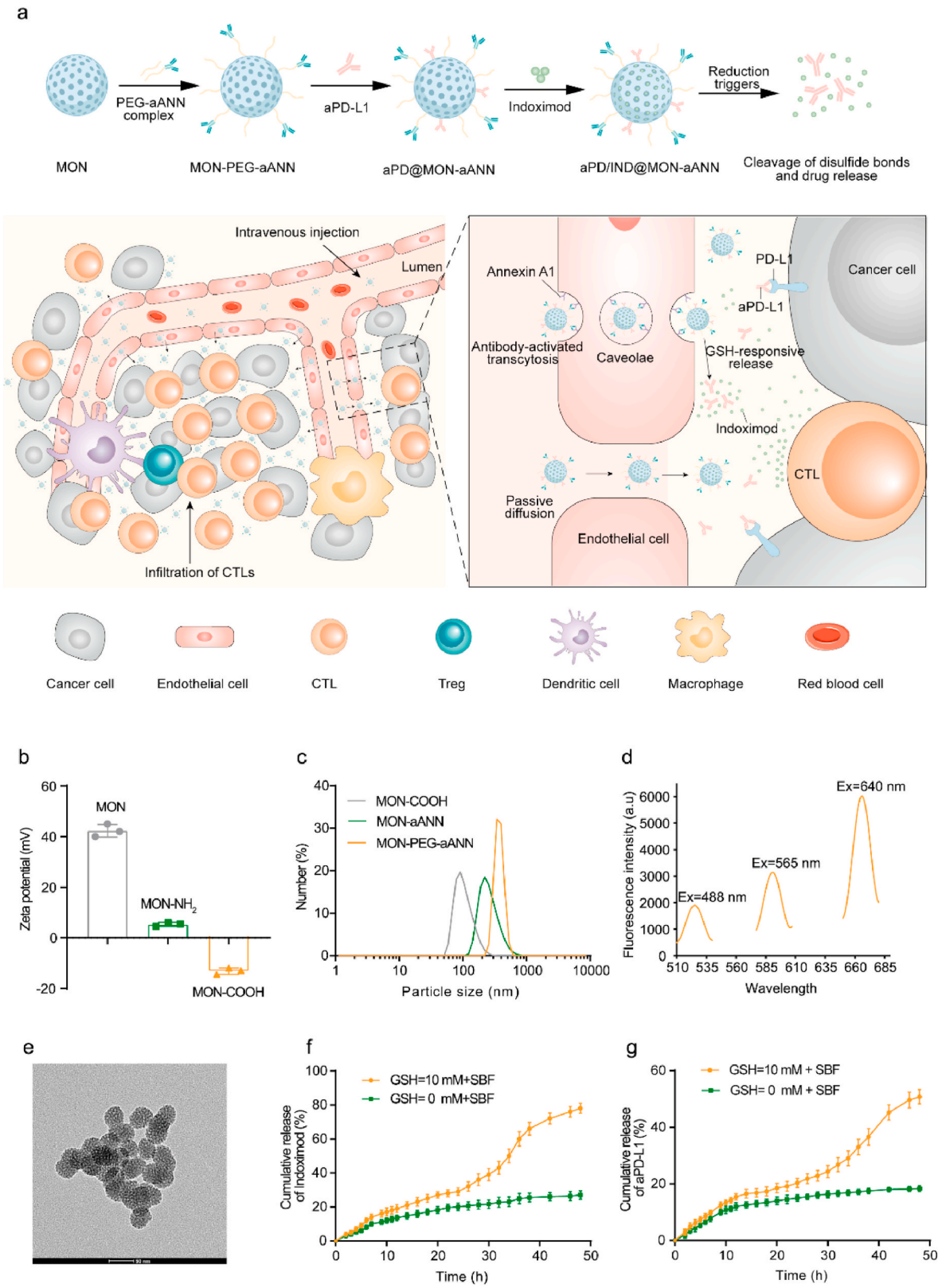

Fig. 1. Scheme and characterization of aPD/IND@MON-aANN nanomedicine. (a)Schematic illustration of aPD/IND@MON-aANN synthesis, ANXA1 antibody-activated *trans*-endothelial transcytosis to augment nanomedicine extravasation and the efficacy of cancer immunotherapy by synergistic modulation of the tumor microenvironment. (b)The zeta potential of MON, MON-NH_2 and MON-COOH measured by DLS. (c) The hydrodynamic size of MON-COOH, MON-aANN and MON-PEG-aANN measured by DLS. (d) Fluorescence emission spectra of aPD@MON-aANN with FITC- labelled MON, PE-labelled aPD-L1 and IRDye 680RD-labelled aANXA1. (e) Representative TEM image of aPD/IND@MON-aANN nanoparticles. Scale bar = 50 nm. (f,g) The release profile of Indoximod (f) and aPD-L1 (g) of aPD/IND@MON-aANN examined in pure SBF or SBF with 10 mM GSH in 48 h.

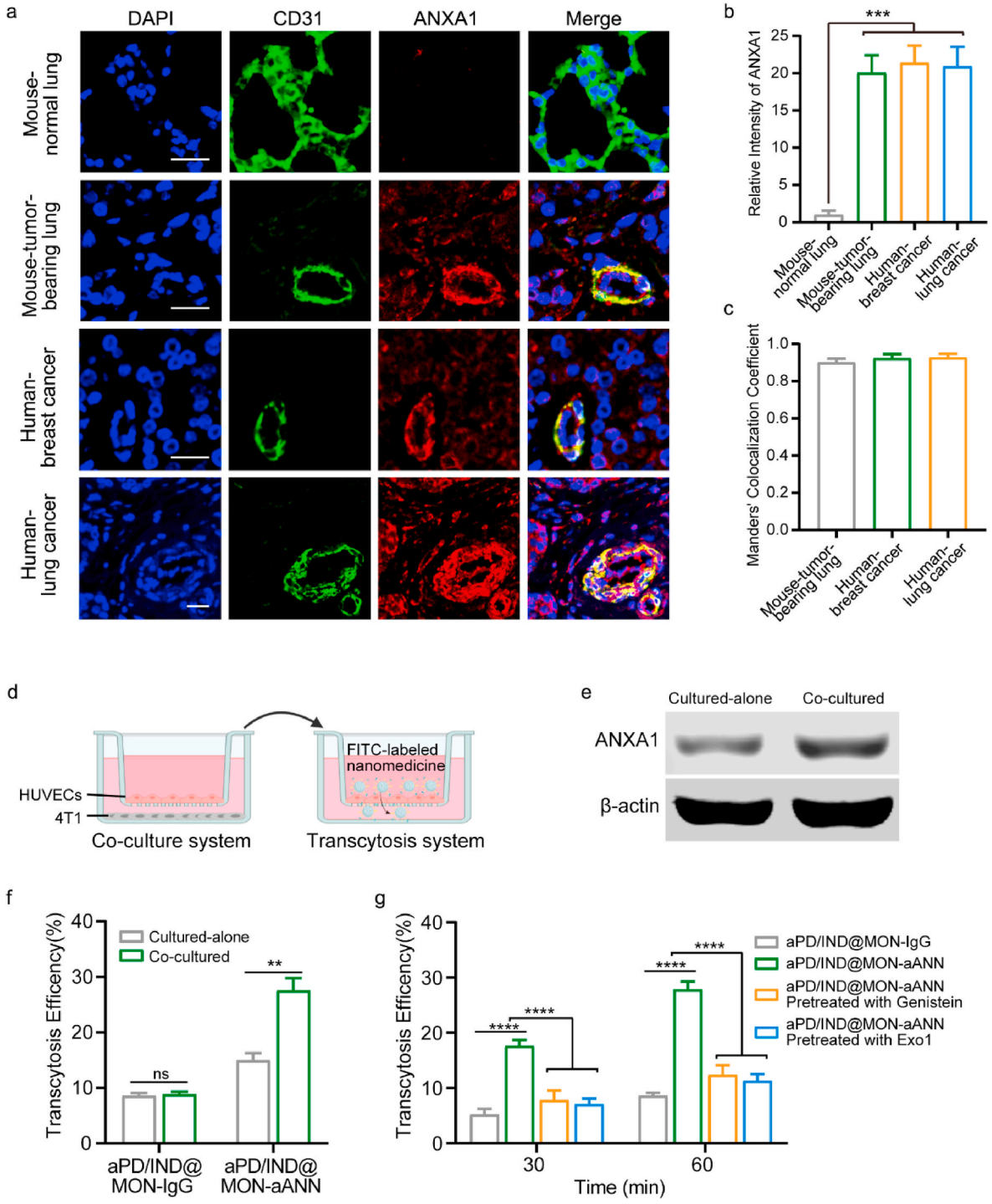

Fig. 2. *in vitro* nanoparticle transcytosis across tumor endothelial cells. (a) Representative immunofluorescence images of CD31 (green) and ANXA1 (red) of various tumor tissue samples with the colocalization shown in yellow color. Scale bar = 20 μm. (b) Quantitative analysis of ANXA1 fluorescence intensity in the CD31 positive zone for various tissue samples (n = 9 images from three independent experiments, data presented as mean ± s.d, one-way ANOVA with Tukey test, ***P < 0.001). (c) Quantitative analysis of co-localization between CD31 and ANXA1 fluorescent signals in the tumor tissue sections, Manders' Colocalization Coefficient denotes the fraction of CD31 overlapping with ANXA1. The coefficient is close to 1 when they are highly co-localized (n = 9 images from three independent experiments). (d) Illustration of the co-culture system between HUVECs and 4T1 tumor cells and transcytosis assay model. (e) Representative western blotting result of ANXA1 in HUVECs cultured alone or co-cultured with 4T1 cells. (f) Transcytosis efficiency of FITC-labelled aPD/IND@MON-IgG and aPD/IND@MON-aANN at 60 min in the transcytosis model with HUVECs cultured alone or pretreated with 4T1 co-culture (n = 3, data presented as mean ± s.d, one-way ANOVA with Tukey test, *P < 0.05, **P < 0.01, ***P < 0.001, ****P < 0.0001). (g) Transcytosis efficiency of FITC-labelled aPD/IND@MON-IgG and aPD/IND@MON-aANN at 30 min and 60 min in the transcytosis model pretreated with or without 200 μM genistein (endocytic pathway inhibitor) or 20 μM EXO1 (exocytic pathway inhibitor) (n = 3, data presented as mean ± s.d, one-way ANOVA with Tukey test, *P < 0.05, **P < 0.01, ***P < 0.001, ****P < 0.0001).

2.17. Cell viability assay

293T cells, NIH-3T3 cells and HUVECs were cultured in 96-well plates at a density of 1×10^4 cells/well. When cells reached approximately 70% of confluency, MON-PEG-aANN nanoparticles were added at various concentrations and incubated for 24 h. Then cell viability was detected by CCK-8 assay according to manufacturer's instructions (Varioskan Flash, Thermo Scientific).

2.18. Biocompatibility and safety evaluation in vivo

The biocompatibility safety of the nanoparticles was further evaluated in naive BALB/c mice. The mice were intravenously injected with PBS, aPD/IND (10 mg kg-1) and aPD/IND@MON-aANN (0.5 mg kg-1) (n = 5 for each group). The blood of the mice was collected at 6, 12, 24 and 48 h to analyze the kinetics of serum ALT and AST level. After 48 h, the mice were sacrificed and the blood was collected to analyze the hematological parameters and serum levels of hepatic, kidney, heart function parameters.

2.19. Statistical analysis

All data were plotted as mean ± standard deviation (s.d). The statistics were analyzed using GraphPad software by one-way analysis of variance (ANOVA) with Tukey's post hoc analysis for multiple comparisons. Differences were considered statistically significant when $P < 0.05$ (*$p < 0.05$, **$p < 0.01$, ***$p < 0.001$, and ****$p < 0.0001$).

3. Results and discussion

3.1. The synthesis and characterization of aPD/IND@MON-aANN

As illustrated in Fig. 1a, in addition to the passive diffusion into tumor interstitium, aANXA1-immobilized mesoporous organosilica nanoparticles (MON) involving aPD-L1 and Indoximod (denoted aPD/IND@MON-aANN) are developed to bind ANXA1 protein on caveolae of luminal tumor endothelial cells and to initiate the endocytosis of nanoparticles via caveolae as well as the subsequently transcellular trafficking of nanocarriers to deliver into abluminal TME. Moreover, aPD-L1 and Indoximod release from aPD/IND@MON-aANN responsive to glutathione (GSH)-mediated reduction and synergistically generate robust anti-tumor immune responses to potentiate the efficacy of immunotherapy for solid tumors. Representative transmission electron microscopy (TEM) image of unmodified mesoporous organosilica nanoparticles (MONs) with framework-incorporated thioether bonds (Fig. S1a, Supporting Information) displayed a spherical morphology with relatively uniform size of ~50 nm, meanwhile evident mesoporous structure could also be observed. The DLS results (Fig. S1b, Supporting Information) demonstrated a uniform size distribution of MONs with a hydrodynamic diameter of 140.8 ± 2.5 nm. Nitrogen adsorption-desorption isotherm results (Figs. S1c and d, Supporting Information) showed that the MONs possessed high surface area of about 429 $m^2 g^{-1}$ and mesoporous structure with a pore size of about 2.1 nm, which makes it optimal as the drug delivery platform [26]. To provide conjugation sites for the following antibody immobilization procedures, amine and carboxy groups were successively introduced to MONs. As indicated by the DLS measurement in Fig. 1b, the MONs decorated with amine groups denoted (MON-NH_2) had a zeta potential of 5.33 ± 0.4 mv, which is less positive than that of raw MONs (42.33 ± 1.5 mv). Meanwhile, after the carboxy functionalization on MON-NH_2 (denoted MON-COOH), the zeta potential of MON-COOH turned into −13.17 ± 0.7 mv. The above zeta potential change suggested the successful sequential grafting of amine and carboxy groups onto raw MONs. So as to immobilize aANXA1 onto MON-COOH and simultaneously improve the stability and the long-circulation property of the nanoparticles [27], heterobifunctional PEG linkers (NH_2-PEG-COOH) were adopted to conjugate aANXA1 and the MON-COOH. Specifically, aANXA1 and the amine ends of PEG linkers were conjugated via reductive amination to form the PEG-aANN complex, which were subsequently used to attach to MON-COOH via EDC/NHS reaction between the carboxy ends on the PEG-aANN complex and the amine groups on MON-COOH. From the DLS results, hydrodynamic diameter of the obtained MON-PEG-aANN nanoparticles was much larger than that of the control MON-aANN group using direct linking method between antibody and MON-COOH, followed by that of MON-COOH (Fig. 1c). The large hydrodynamic size change suggested the attachment of PEG-antibody complex rather than the direct conjugation of antibody onto MONs. This covalent attachment strategy involves the reductive amination of aldehyde-activated sugar moieties within antibody and amines on PEG linkers, making sure the outward orientation of antigen-binding sites of antibodies to maximize the targeting capacity of antibody-installed nanocarriers [21,28]. To verify the therapeutic potential of the nanoplatforms, aPD-L1 was directly immobilized onto MON-PEG-aANN via EDC/NHS-mediated crosslinking and Indoximod was subsequently encapsulated into the mesopores of the nanocarriers (denoted aPD/IND@MON-aANN). For the examination of the attachment of aANXA1 and aPD-L1 on nanocarriers, IRDye 680RD-labelled aANXA1, phycoerythrin (PE)-labelled aPD-L1 and FITC-labelled MON-COOH were used to prepare aPD@MON-aANN. The fluorescence emission spectra of the fluorescently-labelled aPD @MON-aANN (Fig. 1d) manifested the characteristic emission peak at ~526 nm at excitation length of 488 nm, the emission peak at ~592 nm at excitation length of 565 nm and the emission peak at ~667 nm at excitation length of 640 nm, indicating the successful immobilization of both antibodies onto MON-COOH. The grafting efficiency of aPD-L1 was about 30% as determined by ELISA and the encapsulation efficiency of Indoximod in aPD/IND@MON-aANN was about 26.5% by HPLC. From the TEM observation in Fig. 1e, aPD/IND@MON-aANN nanoparticles also exhibited the spherical morphology and mesoporous structure.

Considering the insertion of disulfide bonds into MON framework, the drug release assay of aPD/IND@MON-aANN was conducted in simulated body fluid (SBF) and reductive SBF solution containing 10 mM GSH for 48 h. Indoximod released much faster in reductive SBF than that in pure SBF and displayed a release percentage of ~78% in 48 h (Fig. 1f). Similarly, aPD-L1 released in a reduction-responsive manner and reached ~50% in 48 h in reductive SBF while it exhibited a slow and sustained manner to a release proportion of ~18% in pure SBF during the testing period (Fig. 1g). The accelerated release of the cargos from aPD/IND@MON-aANN in reductive solution suggested that it might be attributed to the responsive degradation of disulfide bonds in nanoparticle framework. However, the in vitro assay for drug release could only extrapolate to the intratumoral drug release behavior and there is possibility that it could not reflect the actual condition in vivo. Furthemore, the TEM images of the products collected at the end of the releasing tests showed that nanoparticles immersed in reductive SBF solution exhibited large number of disintegrated fragments while those in pure SBF presented relatively intact nanoparticle structure and no significant degradation (Fig. S2a, Supporting Information). Similarly, the hydrodynamic size of the products indicated that nanoparticles in reductive SBF had overall smaller size distribution than those in pure SBF (Fig. S2b, Supporting Information). The above results demonstrated that the reduction-responsive degradation of aPD/IND@MON-aANN promoted drug release rate under reductive microenvironment.

3.2. Enhanced tumor extravasation via trans-endothelial pathway

Next, the expression of ANXA1 on tumor endothelium was examined to verify the existence of the target protein of the aANXA1-installed nanoparticles. The representative immunofluorescence staining images of ANXA1 and CD31 (an endothelium marker) for tissue sections from mouse normal lung tissue and various tumor samples were presented in Fig. 2a. The relative ANXA1 fluorescence intensity in the CD31 positive zone for all types of tumor tissue samples were about ~20 fold higher

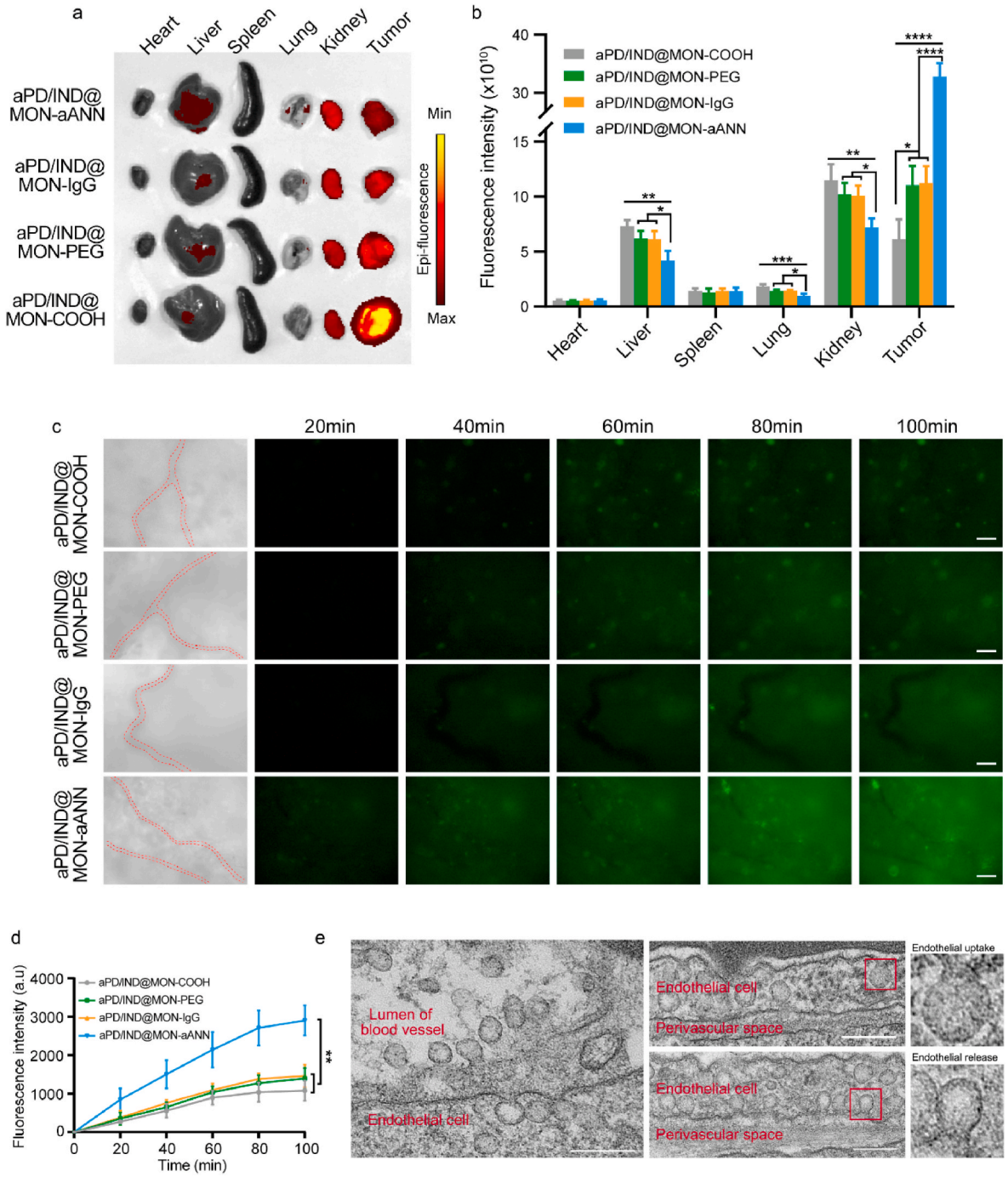

Fig. 3. Enhanced nanoparticle extravasation across tumor endothelium *in vivo*. (a,b) Biodistribution of various Cy5-labelled nanoparticles in major organs and subcutaneous tumor tissues 8 h after intravenous administration (a) and the quantitative fluorescence analysis (b) (n = 3, data presented as mean ± s.d, one-way ANOVA with Tukey test, *P < 0.05, **P < 0.01, ***P < 0.001, ****P < 0.0001). (c) Fluorescent images of time-dependent extravasation and accumulation of aPD/IND@MON-COOH, aPD/IND@MON-PEG, aPD/IND@MON-IgG and aPD/IND@MON-aANN in 4T1 tumors at ears of nude mice. The red dashed lines indicates the tumor blood vessels. Scale bar = 200 μm. (d) The fluorescence intensity of various nanoparticles accumulated in tumor tissues in time-dependent manner (data presented as mean ± s.d, n = 3, one-way ANOVA with Tukey test,**p < 0.01.). (e) Representative TEM images of the microstructure of tumor endothelium and perivascular tissue from tumor-bearing mice intravenously administered with gold-conjugated aPD/IND@MON-aANN. Scale bar = 200 nm.

than that for the normal lung tissue samples (Fig. 2b), indicating the specifically higher expression of ANXA1 in these tumor endotheliums. Furthermore, the colocalization of CD31 (green) and ANXA1 (red) is shown in yellow color in the representative images. A high occurrence of the colocalization of ANXA1 and CD31 could be observed from these tumor sections. Moreover, the Manders' Colocalization Coefficient of the tumor tissue sections were all over 0.85 (Fig. 2c), suggesting the high prevalence of ANXA1 on the endothelial cells. Therefore, these results corroborated the expression of ANXA1 on tumor endothelium in varying types of cancers, indicating the feasibility for aANXA1-decorated nanoplatforms to target at tumor vasculatures. The active *trans*-endothelial transport of the aANXA1-decorated nanomedicine were determined via the co-culture system and the in vitro transcytosis model as illustrated in Fig. 2d. In order to better simulate the tumor endothelial cells that had high expression of ANXA1, we established the co-culture system between HUVECs and 4T1 tumor cells to induce ANXA1

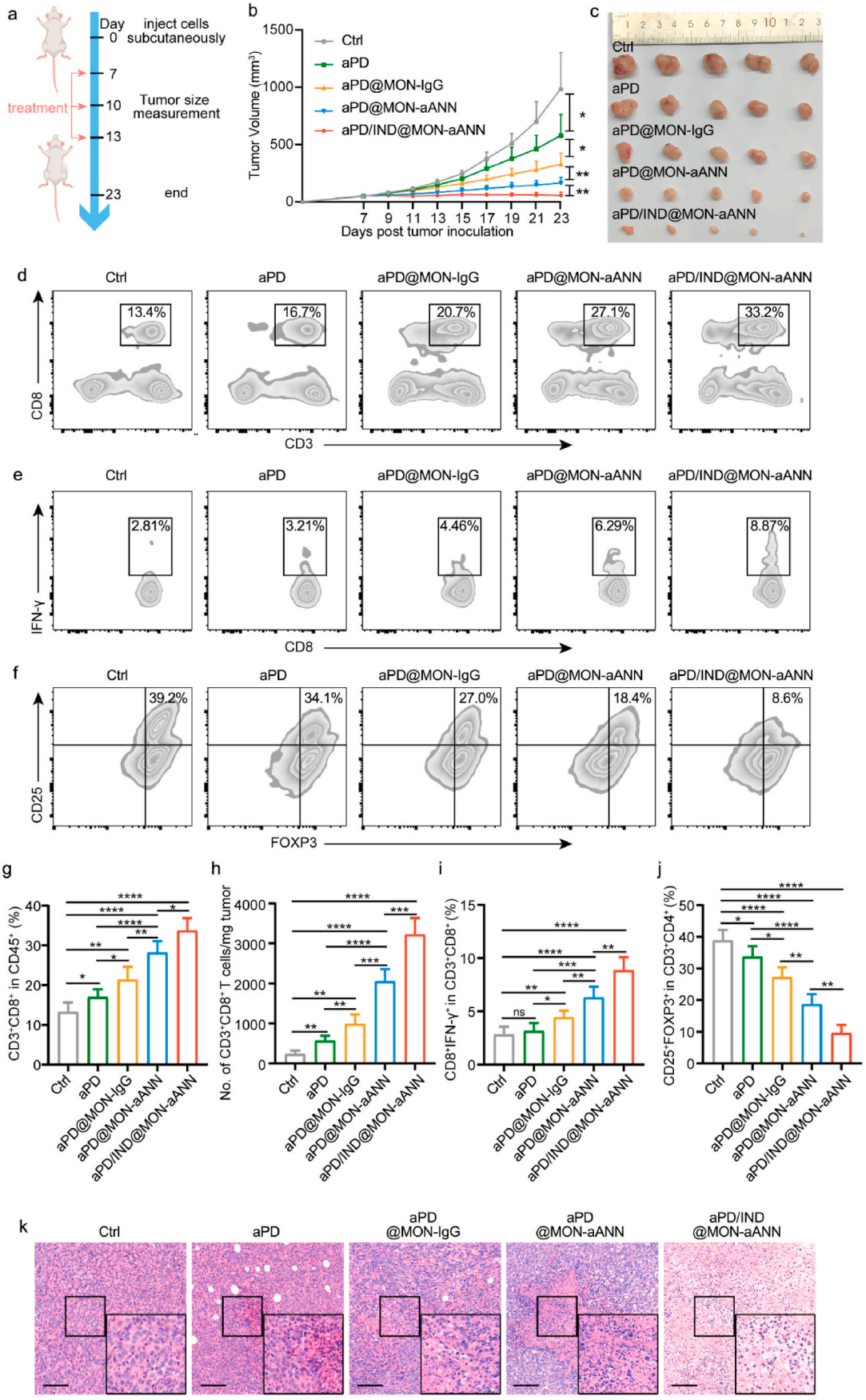

(caption on next page)

Fig. 4. Anti-tumor efficacy and intratumoral immune responses of subcutaneous 4T1 tumors. (a)The therapeutic regime for BALB/c mice subcutaneously inoculated with 5×10^5 4T1 cells per mouse. (b,c) Average tumor growth curves, (b) (n = 5, data presented as mean ± s.d, one-way ANOVA with Tukey test, *P < 0.05, **P < 0.01) and individual tumor images (c) of tumors dissected from animals on the end of study. (d,g) Representative flow cytometric plots (d) and quantitative analysis (g) of intratumoral $CD3^+CD8^+$ subsets within $CD45^+$ T cells (n = 5, data presented as mean ± s.d, one-way ANOVA with Tukey test, *P < 0.05, **P < 0.01, ****P < 0.0001). (h) Number of intratumoral infiltration $CD3^+CD8^+$ T cells per mg of tumor (n = 5, data presented as mean ± s.d, one-way ANOVA with Tukey test, **P < 0.01, ***P < 0.001, ****P < 0.0001). (e,i) Representative flow cytometric plots (e) and quantitative analysis (i) of intratumoral $CD8^+$ IFN-γ^+ T effector subsets (n = 5, data presented as mean ± s.d,one-way ANOVA with Tukey test, ns stand for no significance, *P < 0.05, **P < 0.01, ***P < 0.001, ****P < 0.0001). (f,j) Representative flow cytometric plots (f) and quantitative analysis (j) of intratumoral Treg ($CD4^+CD25^+$ $FOXP3^+$) subsets (n = 5, data presented as mean ± s.d, one-way ANOVA with Tukey test, *P < 0.05, **P < 0.01, ****P < 0.0001). (k) Histological analysis of various tumor tissue sections collected at the study endpoint by H&E staining assay. scale bar = 100 μm. Data were analyzed by one-way ANOVA with Tukey test.

expression in HUVECs and the western blotting result in Fig. 2e confirmed the upregulation of ANXA1 expression in the co-cultured HUVECs compared with those cultured alone. As shown in Fig. 2f, aPD/IND@MON-aANN had significantly higher transcytosis efficiency across the co-cultured HUVECs with high ANXA1 expression while the aPD/IND@MON-IgG group exhibited negligible difference in transcytosis across HUVECs with whether low or high ANXA1 expression, indicating that the aANXA1-conjugated nanomedicine target at the ANXA1 on endothelial cells to distinctly enhance the transcellular transport. In addition, the transcytosis efficiency of aPD/IND@MON-aANN across co-cultured HUVECs pretreated with 200 μM genistein (endocytic pathway inhibitor) or 20 μM EXO1 (exocytic pathway inhibitor) was both significantly diminished (Fig. 2g), suggesting that aANXA1-immobilized nanomedicine traverse the tumor endothelial cells through the active transcytosis pathway.

Next, we performed the biodistribution of various Cy5-labelled nanoparticles 8 h post injection in subcutaneous 4T1 tumor-bearing mice (Fig. 3a and b). Compared with the other formulations, aPD/IND@MON-aANN was shown to preferentially target at tumors with much less accumulation in kidneys, livers and lungs, which indicated that the aANXA1-decorated nanomedicine significantly improved the drug delivery efficiency. The real time *trans*-vascular extravasation and tumor accumulation of FITC-labelled nanomedicines were monitored by fluorescence microscopy as previously described [24]. From the fluorescence images in Fig. 3c and the corresponding quantitative analysis in Fig. 3d, aPD/IND@MON-aANN was found to rapidly transport across the endothelium and evidently accumulate in tumors 20 min after intravenous injection while the other groups exhibited weak fluorescent signals in tumor sites. Moreover, aPD/IND@MON-aANN continued to percolate extensively into tumor interstitium and the fluorescent signal was pervasive throughout most of the tumor tissue at 80 min, exhibiting significantly higher fluorescence intensity relative to the other groups. aPD/IND@MON-IgG and aPD/IND@MON-PEG group displayed a moderate fluorescence intensity since 40 min and the signals of the two groups were slightly higher than those of aPD/IND@MON during the entire test. These results demonstrated that aPD/IND@MON-aANN possessed prominent capacity in extravasation into solid tumors and aANXA1 immobilization contributed to the efficient nanoparticle transport across tumor endothelium to amass in tumor tissue. Furthermore, to ascertain the role of caveolae in mediating the remarkable improvement of aPD/IND@MON-aANN in tumor extravasation, tumor bearing mice were intravenously injected with aPD/IND@MON-aANN nanoparticles with 6 nm colloidal gold nanoparticles attached to aANXA1, followed by TEM observation of the microstructure and contents of caveolae in tissue sections from tumor area. As shown in Fig. 3e, gold-conjugated nanoparticles were observed in the lumen of tumor blood vessel, uptaken by the typical flask-shaped vesicles — caveolae on the luminal endothelium surface [5], subsequently subjected to endocytosis into the endothelial cell and the release from caveolae on abluminal surface to the perivascular space. Taken together, aPD/IND@MON-aANN targeted at caveolar ANXA1 of tumor endothelium and initiated the active *trans*-endothelial transcytosis via caveolae to transport nanomedicine into tumor tissue, thus remarkably boosting the extravasation and accumulation of nanomedicine in solid tumors.

3.3. Anti-tumor activity and potent intratumoral immunity in vivo

The anti-tumor performance and immune responses in TME of various formulations were examined in the subcutaneous 4T1 breast cancer mouse model. The tumor-bearing mice received Isotype control antibody, free aPD-L1 (denoted aPD), aPD@MON-IgG, aPD@MON-aANN and aPD/IND@MON-aANN nanoparticles on day 7, 10, and 13 after tumor inoculation via tail vein injection as illustrated in Fig. 4a aPD@MON-IgG moderately regressed tumor growth with a tumor inhibition rate higher than that of mice given free aPD-L1 (Fig. 4b and c). Importantly, aPD@MON-aANN nanoparticles inhibited the 4T1 tumor progression 3.5- and 2.0-fold more effectively than aPD and aPD@MON-IgG group, respectively. Moreover, aPD/IND@MON-aANN further notably augmented the antitumor activity, leading to regression of tumor size for 60% of the mice. In addition, the body weight of mice for all groups had no significant decrease during the entire anti-tumor study (Fig. S3, Supporting Information). These results suggested that the aANXA1-installed delivery system for aPD-L1 significantly contributed to the promoted immunotherapeutic effects of aPD-L1 and the additional encapsulation of the immune-regulator Indoximod into the aPD@MON-aANN nanocarriers indeed substantially enhanced the efficacy of aPD-L1 ICB therapy. To evaluate the anti-tumor immune responses underlying the superior therapeutic effects of aANXA1-decorated nanomedicines, flow cytometry and histological analysis of tumor tissues were conducted. From the flow cytometric analysis shown in Fig. 4d, g, aPD@MON-aANN significantly elevated the fraction of $CD8^+$ cytotoxic T lymphocytes (CTLs) to 28.14 ± 2.92%, which is ~1.7 fold to that of aPD group. aPD@MON-aANN also exhibited consistently higher number of $CD3^+CD8^+$ T cells normalized to tumor mass relative to aPD@MON-IgG group (Fig. 4h). The fraction of $CD8^+$IFN-γ^+ T cell is 6.31 ± 1.02% for aPD@MON-aANN and 4.45 ± 0.61% for aPD@MON-IgG (Fig. 4e,i). Notably, the combination therapy via aPD/IND@MON-aANN further generated potent anti-tumor immune responses including the significantly augmented CTL fraction of 33.7 ± 3.18%, and IFN-γ^+-producing $CD8^+$ T cell fraction of 8.85 ± 1.24%. Since regulatory T cells ($CD4^+$ $CD25^+$ $Foxp3^+$ T cells, namely, Tregs) constitute an important immunosuppressive population in TME and their intratumoral infiltration suggests poor clinical prognosis [29], the fraction of Tregs was measured by flow cytometry. The control group was shown to have 37.9 ± 3.34% of Treg infiltration, indicating the immunosuppressive TME for 4T1 tumors (Fig. 4f,j). The aPD@MON-aANN treatment dramatically decreased the fraction of Tregs to 18.7 ± 3.22%, which is also significantly lower than that of aPD@MON-IgG group. Notably, aPD/IND@MON-aANN group further attenuated the Treg frequency to 9.62 ± 2.56%, indicating the effective reverse of the immunosuppressive TME by virtue of Indoximod encapsulation into aPD@MON-aANN. Indoximod, a “tryptophan memetic,” acts directly on immune cells and creates an artificial tryptophan-sufficiency signal to reverse IDO pathway–mediated suppression. Indoximod has shown success and a desirable safety profile in multiple phase I and II studies of advanced solid tumors and various cancers, especially in combination with chemotherapy [30]. Apparently, the combined administration of Indoximod and aPD-L1 on aANXA1-decorated nanoplatforms also yielded desirable anti-tumor efficacy. Moreover, TUNEL and H&E staining results consistently exhibited that aPD@MON-aANN and

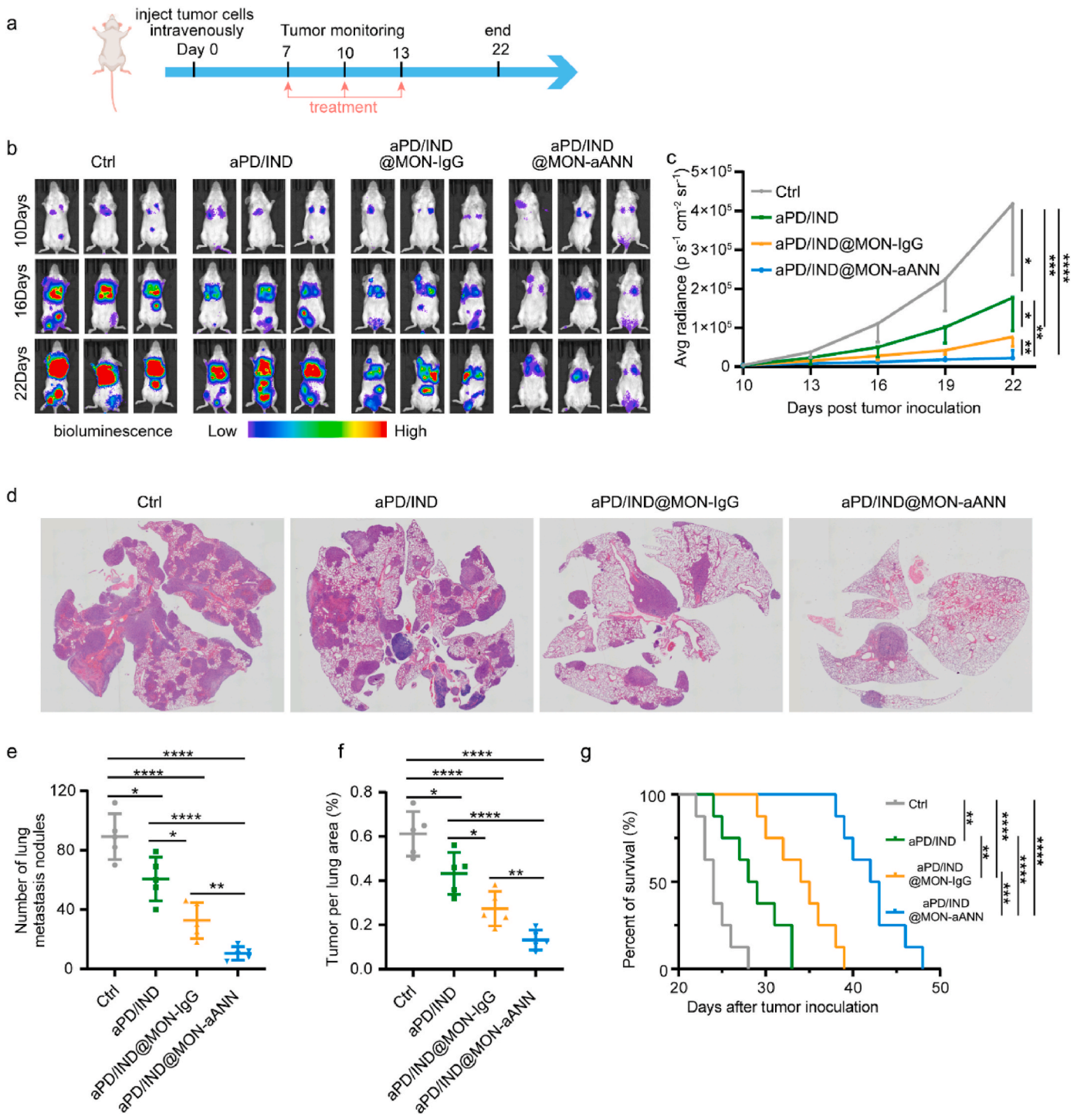

Fig. 5. Anti-metastasis efficacy in 4T1-induced metastatic model. (a) The therapeutic regime for BALB/c mice inoculated with 5×10^5 4T1-luciferase cells per mouse via tail vein injection. (b, c) In vivo bioluminescence images of anaesthetized tumor-bearing mice (b) and the average bioluminescence intensity of various groups at different time points (c) (n = 5, data presented as mean ± s.d,one-way ANOVA with Tukey test, *P < 0.05, **P < 0.01, ***P < 0.001, ****P < 0.0001). (d) Representative H&E staining images of lung tissues from various groups. (e,f) Analysis of the number (e) and tumor area (f) of lung metastasis nodules after various treatments (n = 5, data presented as mean ± s.d, one-way ANOVA with Tukey test, *P < 0.05, **P < 0.01, ****P < 0.0001). (g) Survival curves for various groups (n = 8, log-rank test, **P < 0.01, ***P < 0.001, ****P < 0.0001).

aPD/IND@MON-aANN group both caused much more apoptosis and/or necrosis of tumor cells than the other groups (Fig. 4k and Fig. S4, Supporting Information), which might be attributed to the increased intratumoral infiltration of CTLs and secreted pro-inflammatory cytokines, such as IFN-γ [31]. The above results validated that aPD@MON-aANN nanoparticles significantly promoted the anti-tumor immune responses for ICB therapy whilst the combination nanomedicine of aPD/IND@MON-aANN elicited much more robust anti-tumor immunity and reversed the immunosuppressive TME to further substantially augment the efficacy of ICB immunotherapy for the 4T1 tumor-bearing mice.

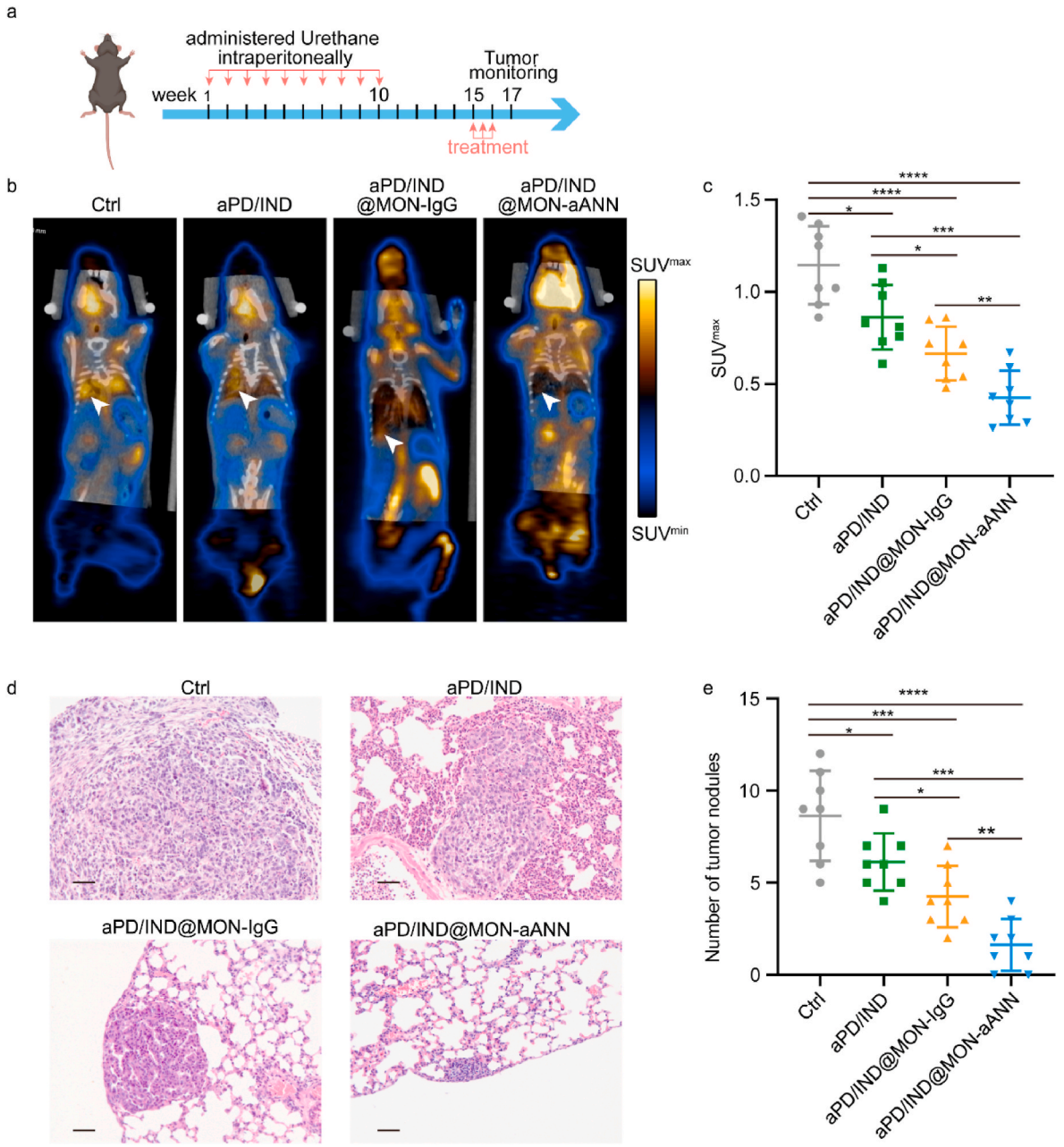

Fig. 6. Anti-tumor activity in orthotopic lung cancer model. (a) The therapeutic regime for C57BL/6 mice with orthotopic lung cancers induced by urethane. (b) Representative 18F-FDG micro-PET/CT images of tumor-bearing mice after various treatments. The arrows represent tumor signals. (c) Analysis of SUV^{max} value for various groups (n = 8, data presented as mean ± s.d, Data were analyzed by one-way ANOVA with Tukey test, *P < 0.05, **P < 0.01, ***P < 0.001, ****P < 0.0001). (d) Representative H&E-stained sections of lung tissues of various groups. Scale bar = 50 μm. (e) Analysis of the number of tumor nodules in lung-tissue sections from mice treated with various formulations (n = 8, data presented as mean ± s.d, Data were analyzed by one-way ANOVA with Tukey test, *P < 0.05, **P < 0.01, ***P < 0.001, ****P < 0.0001).

3.4. Inhibition of 4T1 tumor metastasis

Immunosuppressive microenvironment in tumors could enhance tumor immune escape and further facilitate tumor metastasis via inducing immunosuppression, enhancing tumor cell invasion and intravasation, forming a pre-metastatic niche and etc. [32], meanwhile metastasis is the major reason for mortality caused by breast cancer, [33]. It has been reported that premetastatic niche in rapidly progressing 4T1 breast cancers had abundant angiogenesis process [34], thus the aANXA1-decorated nanomedicine by virtue of active *trans*-endothelial transcytosis exerts great potential in delivering immunotherapeutics to diminishing metastasis. Therefore, the anti-metastatic potential of aPD/IND@MON-aANN nanoparticles were further assessed. Grouped female BALB/c mice were inoculated with 4T1-luciferase breast cancer cells via tail vein injection, followed by intravenous administration of Isotype control antibody, free aPD-L1 and Indoximod (denoted aPD/IND), aPD/IND@MON-IgG and aPD/IND@MON-aANN nanoparticles on day 7, 10 and 13 (Fig. 5a). The tumor metastasis of the mice was detected by in vivo imaging system (IVIS) and mice were sacrificed when the bioluminescence of any group exceeded 5×10^5 p $s^{-1}cm^{-2}sr^{-1}$. The main organs of the sacrificed mice were then collected for H&E staining to confirm tumor metastasis (Fig. S5, Supporting Information). As indicated by the bioluminescence results (Fig. 5b, c) and H&E staining images of lung tissue sections (Fig. 5d–f), free aPD/IND

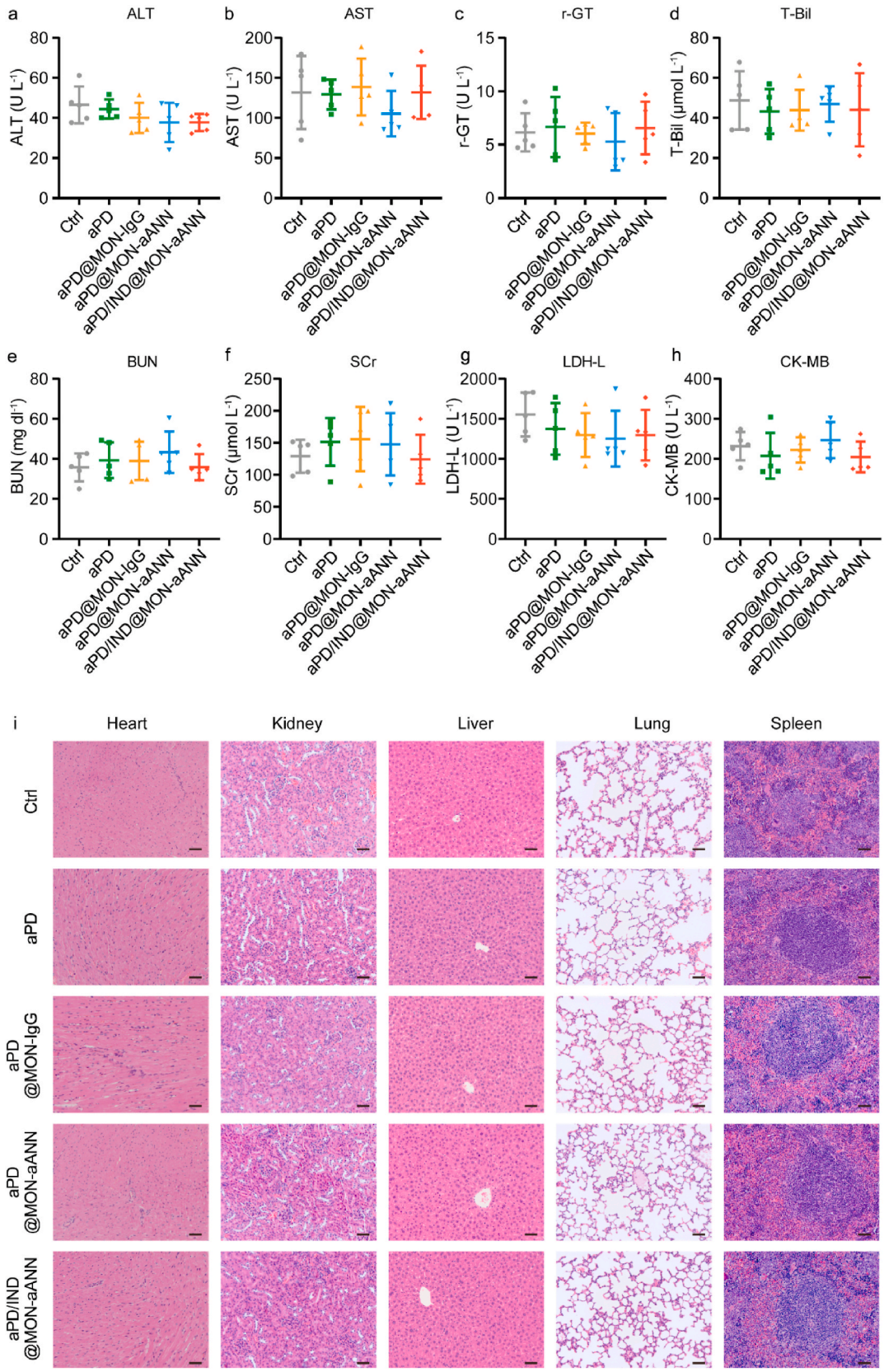

Fig. 7. Biocompatibility and safety evaluation. (a-h) The level of ALT (a), AST (b), r-GT (c), T-Bil (d), BUN (e), SCr (f), LDH-L (g) and CK-MB (h) in the serum from subcutaneous tumor-bearing mice at the endpoint of therapeutic study (n = 5, data presented as mean ± s.d). (i) Representative H&E-stained sections of heart, kidney, liver, lung and spleen from mice of different groups. Scale bar = 50 μm.

administration moderately regressed tumor metastasis and aPD/IND@MON-IgG nanomedicine displayed enhanced anti-metastasis effects compared with free aPD/IND. Of note, aPD/IND@MON-aANN markedly diminished the metastasis level including significant reduction in systemic bioluminescence signals as well as the number and area of lung metastasis nodules relative to aPD/IND@MON-IgG group. The survival study was adopted to evaluate the comprehensive therapeutic effects of various formulations (Fig. 5g). Mice treated with aPD/IND@MON-aANN exhibited a prominently longer median survival time to 42.5 days as compared with those received Isotype control antibody (24 days, $P < 0.0001$), aPD/IND (28.5 days, $P < 0.0001$) and aPD/IND@MON-IgG (34.5 days, $P < 0.001$).

3.5. Anti-tumor efficacy in orthotopic lung cancer

Since lung cancers also develop in a context of tumor-induced immune suppression [35], we established the urethane-induced orthotopic lung cancer mouse model to further explore the general applicability of aPD/IND@MON-aANN nanoplatforms. Mice were administered intraperitoneally with urethane per week (1 mg g^{-1} body weight) for 10 consecutive doses as described previously [25]. 15 weeks after the first dosage, tumor-bearing mice were randomly grouped and intravenously treated with Isotype control antibody, aPD/IND, aPD/IND@MON-IgG and aPD/IND@MON-aANN every 3 days for 3 times as illustrated in Fig. 6a. 2 weeks after the first treatment, tumor progression was assessed by 18F-FDG microPET/CT and the lung tissue of the sacrificed mice were dissected for H&E staining to further verify the tumor progression. The 18F-FDG microPET/CT imaging and corresponding quantitative results (Fig. 6b and c) manifested that there was significantly lower SUV^{max} value for aPD/IND@MON-aANN group than that for the other groups, implying that aPD/IND@MON-aANN nanomedicine effectively postponed the progression of the urethane-induced orthotopic lung cancer. In addition, H&E staining assay (Fig. 6d and e) produced analogous results, with aPD/IND@MON-aANN displaying much lower number of tumor nodules (>100 μm) compared with aPD/IND@MON-IgG and aPD/IND group.

3.6. Biocompatibility and safety evaluation

The biocompatibility and safety analysis of aANXA1-decorated nanoparticles was also evaluated in vitro and in vivo. After incubation with the nanoparticles for 24 h, the viability of NIH-3T3, 293T cells and HUVECs were determined by Cell Counting Kit-8 (CCK-8). The results showed that both cell types displayed a viability of over 90% without being damaged by the increase of nanoparticle concentration (Fig. S6, Supporting Information). The in vivo biocompatibility was confirmed by the stable body weight statistics (Fig. S3, Supporting Information) for all groups throughout the therapeutic assays for subcutaneous tumor-bearing mice. Moreover, the serum hepatic enzyme parameters (alanine aminotransferase (ALT)/aspartate aminotransferase (AST)/Gamma-glutamyl transpeptidase (γ-GT)/total bilirubin (T-Bil)), kidney function indexes (blood urea nitrogen (BUN) and serum creatinine (SCr)) and heart function indexes (lactic dehydrogenase (LDH-L) and creatine kinase-myocardial band (CK-MB)) were all within the reference values at the endpoint of the study (Fig. 7a–h). In addition, there were no obvious damages in major organs as indicated by H&E-stained tissue sections, (Fig. 7i). Additionally, the aPD/IND, and aPD/IND@MON-aANN were injected into naïve mice and there was no significant difference in the above-mentioned major organ function parameters and hematological parameters, including the content of hemoglobin and the number of white blood cells, red blood cells and platelets (Figs. S7a–j, Supporting Information). The kinetics of serum ALT and AST level in (Fig. S7k,l, Supporting Information) indicated that the ALT and AST levels of aPD/IND, and aPD/IND@MON-aANN group were both slightly higher than the PBS group but still within the reference values. The above results demonstrated the satisfying in vivo biocompatibility and safety of the nanoparticles.

4. Conclusion

In summary, we propose ANXA1 antibody-installed reduction-responsive mesoporous organosilica nanoplatforms involving combination immuno-therapeutics of aPD-L1 and Indoximod to efficiently enhance nanomedicine extravasation via the antibody-triggered active *trans*-endothelial delivery route, thus distinctly augmenting the immunotherapy efficacy for solid tumors. Particularly, the immobilized aANXA1 on the nanoplatforms serve to target at the caveolar ANXA1 protein of luminal endothelial cells and to activate endocytosis and transcytosis of nanomedicine mediated by caveolae to transport across tumor endothelial cells, resulting in rapid and substantial nanoparticle extravasation and accumulation in TME. Moreover, aPD-L1 and Indoximod release from aPD/IND@MON-aANN nanoplatforms in a reduction-responsive manner and cooperatively elicit potent anti-tumor immune responses including improving the intratumoral infiltration and activation of CTLs and reducing the fraction of Treg subsets. aPD/IND@MON-aANN is demonstrated to exhibit potent anti-tumor effects in subcutaneous 4T1 breast tumors and remarkable anti-metastatic performance in 4T1 metastasis model. Compared with combination administration of free drugs, aPD/IND@MON-aANN nanomedicine presents much more robust therapeutic efficacy to attenuate the progression of urethane-induced orthotopic lung cancers in mice. Therefore, aPD/IND@MON-aANN nanomedicine with superior delivery efficiency via active *trans*-endothelial transcytosis as well as potent immunotherapeutic capacity may exert tremendous potential for the treatment of a range of solid tumors.

CRediT authorship contribution statement

Tinglei Huang: Formal analysis, Data curation, Writing - original draft, designed experiments, analy. **Shuang Li:** Formal analysis, Data curation, Writing - original draft, designed experiments, analy. **Jianchen Fang:** performed the experiments. **Fuli Li:** performed the experiments. All of the authors agreed to submit the final manuscript. **Shuiping Tu:** Supervision, provided overall scientific guidance and supervised the scientific work. All of the authors agreed to submit the final manuscript.

Declaration of competing interest

None.

Acknowledgements

This work was financially supported by the National Natural Science Foundation of China (NSFC 81472727, NSFC 81773259 and NSFC 91029718); Science and Technology Commission of Shanghai Municipality (15JC1403100); National laboratory of Oncogene and Cancer-related Genes foundation (90-15-05).

Appendix A. Supplementary data

Supplementary data to this article can be found online at https://doi.org/10.1016/j.bioactmat.2020.12.023.

References

[1] L. Salvioni, M.A. Rizzuto, J.A. Bertolini, L. Pandolfi, M. Colombo, D. Prosperi, Thirty years of cancer nanomedicine: success, frustration, and hope, Cancers 11 (12) (2019), https://doi.org/10.3390/cancers11121855.
[2] J. Shi, P.W. Kantoff, R. Wooster, O.C. Farokhzad, Cancer nanomedicine: progress, challenges and opportunities, Nat. Rev. Canc. 17 (1) (2017) 20–37, https://doi.org/10.1038/nrc.2016.108.

[3] H. He, L. Liu, E.E. Morin, M. Liu, A. Schwendeman, Survey of clinical translation of cancer nanomedicines-lessons learned from successes and failures, Acc. Chem. Res. 52 (9) (2019) 2445–2461, https://doi.org/10.1021/acs.accounts.9b00228.
[4] S. Wilhelm, A.J. Tavares, Q. Dai, S. Ohta, J. Audet, H.F. Dvorak, W.C.W. Chan, Analysis of nanoparticle delivery to tumours, Nature Reviews Materials 1 (5) (2016) 16014, https://doi.org/10.1038/natrevmats.2016.14.
[5] S.M. Kim, P.H. Faix, J.E. Schnitzer, Overcoming key biological barriers to cancer drug delivery and efficacy, J. Contr. Release : official journal of the Controlled Release Society 267 (2017) 15–30, https://doi.org/10.1016/j.jconrel.2017.09.016.
[6] S.K. Golombek, J.N. May, B. Theek, L. Appold, N. Drude, F. Kiessling, T. Lammers, Tumor targeting via EPR: strategies to enhance patient responses, Adv. Drug Deliv. Rev. 130 (2018) 17–38, https://doi.org/10.1016/j.addr.2018.07.007.
[7] H. Nakamura, J. Fang, H. Maeda, Development of next-generation macromolecular drugs based on the EPR effect: challenges and pitfalls, Expet Opin. Drug Deliv. 12 (1) (2015) 53–64, https://doi.org/10.1517/17425247.2014.955011.
[8] S. Sindhwani, A.M. Syed, J. Ngai, B.R. Kingston, L. Maiorino, J. Rothschild, P. MacMillan, Y. Zhang, N.U. Rajesh, T. Hoang, J.L.Y. Wu, S. Wilhelm, A. Zilman, S. Gadde, A. Sulaiman, B. Ouyang, Z. Lin, L. Wang, M. Egeblad, W.C.W. Chan, The entry of nanoparticles into solid tumours, Nat. Mater. 19 (5) (2020) 566–575, https://doi.org/10.1038/s41563-019-0566-2.
[9] Q. Zhou, S. Shao, J. Wang, C. Xu, J. Xiang, Y. Piao, Z. Zhou, Q. Yu, J. Tang, X. Liu, Z. Gan, R. Mo, Z. Gu, Y. Shen, Enzyme-activatable polymer-drug conjugate augments tumour penetration and treatment efficacy, Nat. Nanotechnol. 14 (8) (2019) 799–809, https://doi.org/10.1038/s41565-019-0485-z.
[10] P. Oh, P. Borgström, H. Witkiewicz, Y. Li, B.J. Borgström, A. Chrastina, K. Iwata, K. R. Zinn, R. Baldwin, J.E. Testa, J.E. Schnitzer, Live dynamic imaging of caveolae pumping targeted antibody rapidly and specifically across endothelium in the lung, Nat. Biotechnol. 25 (3) (2007) 327–337, https://doi.org/10.1038/nbt1292.
[11] D.P. McIntosh, X.Y. Tan, P. Oh, J.E. Schnitzer, Targeting endothelium and its dynamic caveolae for tissue-specific transcytosis in vivo: a pathway to overcome cell barriers to drug and gene delivery, Proc. Natl. Acad. Sci. U.S.A. 99 (4) (2002) 1996–2001, https://doi.org/10.1073/pnas.251662398.
[12] P. Oh, Y. Li, J. Yu, E. Durr, K.M. Krasinska, L.A. Carver, J.E. Testa, J.E. Schnitzer, Subtractive proteomic mapping of the endothelial surface in lung and solid tumours for tissue-specific therapy, Nature 429 (6992) (2004) 629–635, https://doi.org/10.1038/nature02580.
[13] P. Mi, H. Cabral, K. Kataoka, Ligand-installed nanocarriers toward precision therapy, Adv. Mater. 32 (13) (2020), e1902604, https://doi.org/10.1002/adma.201902604.
[14] M. Yarchoan, A. Hopkins, E.M. Jaffee, Tumor mutational burden and response rate to PD-1 inhibition, N. Engl. J. Med. 377 (25) (2017) 2500–2501, https://doi.org/10.1056/NEJMc1713444.
[15] B.A. Wilky, Immune checkpoint inhibitors: the linchpins of modern immunotherapy, Immunol. Rev. 290 (1) (2019) 6–23, https://doi.org/10.1111/imr.12766.
[16] M. Binnewies, E.W. Roberts, K. Kersten, V. Chan, D.F. Fearon, M. Merad, L. M. Coussens, D.I. Gabrilovich, S. Ostrand-Rosenberg, C.C. Hedrick, R. H. Vonderheide, M.J. Pittet, R.K. Jain, W. Zou, T.K. Howcroft, E.C. Woodhouse, R. A. Weinberg, M.F. Krummel, Understanding the tumor immune microenvironment (TIME) for effective therapy, Nat. Med. 24 (5) (2018) 541–550, https://doi.org/10.1038/s41591-018-0014-x.
[17] K.G. Anderson, I.M. Stromnes, P.D. Greenberg, Obstacles posed by the tumor microenvironment to T cell activity: a case for synergistic therapies, Canc. Cell 31 (3) (2017) 311–325, https://doi.org/10.1016/j.ccell.2017.02.008.
[18] Y. Shi, T. Lammers, Combining nanomedicine and immunotherapy, Acc. Chem. Res. 52 (6) (2019) 1543–1554, https://doi.org/10.1021/acs.accounts.9b00148.
[19] L. Yu, Y. Chen, H. Lin, W. Du, H. Chen, J. Shi, Ultrasmall mesoporous organosilica nanoparticles: morphology modulations and redox-responsive biodegradability for tumor-specific drug delivery, Biomaterials 161 (2018) 292–305, https://doi.org/10.1016/j.biomaterials.2018.01.046.
[20] Y. Gao, S. Gu, Y. Zhang, X. Xie, T. Yu, Y. Lu, Y. Zhu, W. Chen, H. Zhang, H. Dong, P. J. Sinko, L. Jia, The architecture and function of monoclonal antibody-functionalized mesoporous silica nanoparticles loaded with mifepristone: repurposing abortifacient for cancer metastatic chemoprevention, Small 12 (19) (2016) 2595–2608, https://doi.org/10.1002/smll.201600550.
[21] S. Kumar, J. Aaron, K. Sokolov, Directional conjugation of antibodies to nanoparticles for synthesis of multiplexed optical contrast agents with both delivery and targeting moieties, Nat. Protoc. 3 (2) (2008) 314–320, https://doi.org/10.1038/nprot.2008.1.
[22] L. Cai, C. Yang, W. Jia, Y. Liu, R. Xie, T. Lei, Z. Yang, X. He, R. Tong, H. Gao, Endo/lysosome-escapable delivery depot for improving BBB transcytosis and neuron targeted therapy of alzheimer's disease, Adv. Funct. Mater. 30 (27) (2020) 1909999.
[23] A.J. Clark, M.E. Davis, Increased brain uptake of targeted nanoparticles by adding an acid-cleavable linkage between transferrin and the nanoparticle core, Proc. Natl. Acad. Sci. U.S.A. 112 (40) (2015) 12486–12491.
[24] Y. Wang, W. Song, J. Wang, T. Wang, X. Xiong, Z. Qi, W. Fu, X. Yang, Y.G. Chen, Single-cell transcriptome analysis reveals differential nutrient absorption functions in human intestine, J. Exp. Med. 217 (2) (2020), https://doi.org/10.1084/jem.20191130.
[25] Y.E. Miller, L.D. Dwyer-Nield, R.L. Keith, M. Le, W.A. Franklin, A.M. Malkinson, Induction of a high incidence of lung tumors in C57BL/6 mice with multiple ethyl carbamate injections, Canc. Lett. 198 (2) (2003) 139–144, https://doi.org/10.1016/s0304-3835(03)00309-4.
[26] T.L. Nguyen, Y. Choi, J. Kim, Mesoporous silica as a versatile platform for cancer immunotherapy, Adv. Mater. 31 (34) (2019), e1803953, https://doi.org/10.1002/adma.201803953.
[27] A. Koshkaryev, R. Sawant, M. Deshpande, V. Torchilin, Immunoconjugates and long circulating systems: origins, current state of the art and future directions, Adv. Drug Deliv. Rev. 65 (1) (2013) 24–35, https://doi.org/10.1016/j.addr.2012.08.009.
[28] J.M. Montenegro, V. Grazu, A. Sukhanova, S. Agarwal, J.M. de la Fuente, I. Nabiev, A. Greiner, W.J. Parak, Controlled antibody/(bio-) conjugation of inorganic nanoparticles for targeted delivery, Adv. Drug Deliv. Rev. 65 (5) (2013) 677–688, https://doi.org/10.1016/j.addr.2012.12.003.
[29] S. Sakaguchi, M. Miyara, C.M. Costantino, D.A. Hafler, FOXP3+ regulatory T cells in the human immune system, Nature reviews, Immunology 10 (7) (2010) 490–500, https://doi.org/10.1038/nri2785.
[30] C. Luther, U. Swami, J. Zhang, M. Milhem, Y. Zakharia, Advanced stage melanoma therapies: detailing the present and exploring the future, Crit. Rev. Oncol.-Hematol. 133 (2019) 99–111.
[31] D.W. Kowalczyk, A.P. Wlazlo, W. Giles-Davis, A.R. Kammer, S. Mukhopadhyay, H. C. Ertl, Vaccine-induced CD8+ T cells eliminate tumors by a two-staged attack, Canc. Gene Ther. 10 (12) (2003) 870–878, https://doi.org/10.1038/sj.cgt.7700653.
[32] Y. Liu, X. Cao, Immunosuppressive cells in tumor immune escape and metastasis, J. Mol. Med. (Berl.) 94 (5) (2016) 509–522.
[33] B. Weigelt, J.L. Peterse, L.J. van 't Veer, Breast cancer metastasis: markers and models, Nat. Rev. Canc. 5 (8) (2005) 591–602, https://doi.org/10.1038/nrc1670.
[34] S.M. Ghouse, S.K. Vadrevu, S. Manne, B. Reese, J. Patel, B. Patel, A. Silwal, N. Lodhi, Y. Paterson, S.K. Srivastava, M. Karbowniczek, M.M. Markiewski, Therapeutic targeting of vasculature in the premetastatic and metastatic niches reduces lung metastasis, J. Immunol. 204 (4) (2020) 990–1000.
[35] L. Pyfferoen, P. Mestdagh, K. Vergote, N. De Cabooter, J. Vandesompele, B. N. Lambrecht, K.Y. Vermaelen, Lung tumours reprogram pulmonary dendritic cell immunogenicity at the microRNA level, Int. J. Canc. 135 (12) (2014) 2868–2877.